ACS EARTH AND SPACE CHEMISTRY

http://pubs.acs.org/journal/aesccq Article

Downloaded via LEHIGH UNIV on December 7, 2023 at 16:31:12 (UTC).
See https://pubs.acs.org/sharingguidelines for options on how to legitimately share published articles.

Water Sorption on Formic Acid-Modified Hydroxyapatite as a Function of Relative Humidity: Simulated Environmental Aging Effects on Hygroscopicity and Nutrient Release

Manoj Silva, Mohamed Eisa, Dovilė Ragauskaitė, and Jonas Baltrusaitis*

Cite This: *ACS Earth Space Chem.* 2022, 6, 3043−3053 Read Online

ACCESS | Metrics & More | Article Recommendations

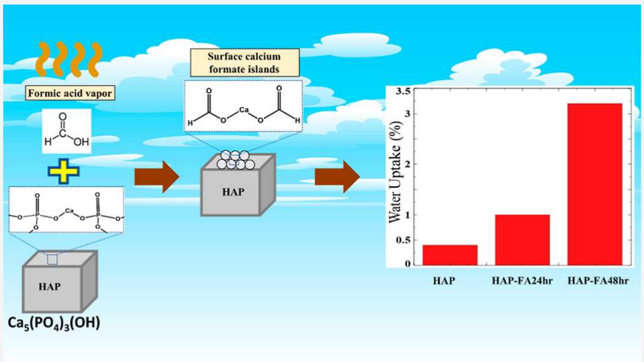

ABSTRACT: Phosphate minerals play an important role in the natural cycle of phosphorous, both in the solid form used in agricultural applications and as aerosolized apatite mineral particles. Mineral surface aging processes, such as organic acid processing, have a significant effect on the phosphate particle physicochemical properties, particularly, their hygroscopicity. In this study, hydroxyapatite was used as a model for low solubility apatite phosphate minerals and subjected to acid processing with formic acid (FA) vapor to simulate the atmospheric processing caused by volatile organic compounds present in the troposphere. Hydroxyapatite particles were shown to react with the FA vapor to form $Ca(HCOO)_2$ on the particle surface, resulting in a heterogeneous microparticle surface, as evidenced by spatially resolved Raman spectroscopy. Due to the more soluble nature of the $Ca(HCOO)_2$ formed on the surface, the hygroscopicity of the acid-processed particle surfaces was shown to increase using dynamic vapor sorption studies. The maximum water uptake at 95% RH was shown to increase from 0.4 to 0.82% and 3.26% after 24 and 48 h of laboratory acid exposure, respectively. Conventional adsorption models, including Brunauer−Emmett−Teller and Freundlich, were used to fit the adsorption data. The heat of sorption values of the 48 h acid-exposed sample was shown to converge to the heat of condensation of water at higher coverage values compared to untreated and 24 h processed hydroxyapatite.

KEYWORDS: *hydroxyapatite, relative humidity, adsorption, Freundlich, BET*

■ INTRODUCTION

The total mass of particulate matter entering the atmosphere is estimated to be between 3000 and 5000 Tg, from which mineral dust is of special interest due to its high propensity to react with trace atmospheric gases and volatile organic compounds, resulting in atmospheric processing (aging) of these particles.[1,2] Such atmospheric processing can cause various physicochemical transformations in the mineral dust particles by changing their hygroscopic properties.[3,4] These transformations that occur in the troposphere have potential impacts on chemical cycles and trace gas concentrations by providing a reactive surface for various heterogeneous reactions.[5] Particles entering the atmosphere can be of natural or anthropogenic sources and contribute significant sources of nutrients to the environment through the many atmospheric aging reactions that occur.[6] In particular, the reactions occurring on mineral dust interfaces with volatile organic compounds (VOCs) have been of great interest due to the implications these reaction hold for climate change and air quality affecting human health.[7,8] Biogenic sources emit the majority of global VOC emissions (~1150 Tg), but anthropogenic emissions despite being smaller globally (~100 Tg), in urban areas, the local VOC emissions can often be higher in quantity[9] since the presence of mineral dust in the troposphere can serve as reactive surfaces for condensation of such VOCs that would alter the surface properties of mineral dust.[10]

Phosphorous-bearing minerals play an important role in the P-cycle as they can contribute to P deposition into the ocean which increases the amount of bioavailable P in the ocean.[11] Saharan dust in particular is rich in Ca-bound P.[12] The P release rate from aerosol particles can be affected by organic ligands, UV light, and acid processes.[13] Apatite minerals [such as hydroxyapatite (HAP)] are the primary form of P-bearing

Received: September 3, 2022
Revised: November 3, 2022
Accepted: November 3, 2022
Published: November 15, 2022

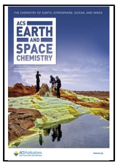

© 2022 American Chemical Society

https://doi.org/10.1021/acsearthspacechem.2c00273

mineral aerosols, and their P release rate is primarily affected by acid processing as apatites are not photoactive and Ca is not strongly complexed by organic ligands.[14] HAP is an especially important environmentally relevant phosphorus-bearing mineral due to its emerging use in agriculture as a novel slow-release fertilizer material.[15] The solubility product constant, K_{sp}, of HAP is reported to be 2.9×10^{-58}, resulting in a low solubility under varying environmental conditions for long periods and release of P-nutrient at a slow rate.[16−18] Sorption of volatile organic acids such as tropospherically abundant formic acid (FA) has been studied on the HAP surface, with a specific focus on (001) and (010) facets.[19] The FA was shown to dissociate and form strong interaction between $HCOO^-$ ions and the Ca^{2+} on the HAP surface.[19] Acid-processing of HAP has clear implications on its inorganic P release and as such, the study of surface properties of volatile organic acid-processed HAP has significant potential for understanding environmental transformations of acid-modified P-bearing mineral interfaces. While the water sorption properties of HAP and whether acid-processed HAP shows significant deviations in water sorption compared to unmodified HAP is a research area of high importance, very few reported insights are available. The literature on water sorption on HAP is limited, with some recent work focusing on understanding the effect of particle size on the number of adsorbed water layers on nano-HAP, as well as the Ca/P ratio, which tunes surface properties.[17,18] Furthermore, recent work on water sorption on HAP has shown that the water sorption isotherm-derived data are well-fitted to Brunauer−Emmett−Teller (BET) and Freundlich models.[20] The water sorption properties of minerals are highly dependent on the surface composition, and as such, the surface modifications caused by VOC reactions become a key parameter in understanding the interactions between water vapor and VOC-reacted mineral dust.

This work is focused on understanding how the water sorption properties and the surface chemistry of HAP are affected by exposure to a volatile organic acid, which is aimed at modeling the heterogeneous reactions that occur on P-bearing mineral dust in the troposphere. FA was chosen as the model molecule to study this phenomenon due to its volatility. Dynamic vapor sorption (DVS) was utilized to study the water uptake as a function of relative humidity (RH). Further characterization of the HAP and FA-modified HAP was performed using X-ray diffraction (XRD), Raman spectroscopy, scanning electron microscopy (SEM), and diffuse reflectance infrared spectroscopy (DRIFTS).

■ MATERIALS AND METHODS

Materials. The HAP was obtained from Millipore-Sigma (99%). FA was obtained from Fischer Scientific.

FA Processing of HAP Particle Surfaces. The HAP particles were sealed in a glass chamber mounted above the saturated FA aqueous solution for 24 or 48 h in an accelerated aging procedure. The FA solution was obtained by diluting FA into a 20% (by volume) solution with deionized water. After the specified exposure time, the sample was removed and used without further treatments.

Powder X-ray Diffraction. The powder XRD patterns were acquired using an Empyrean, PANalytical B.V. diffractometer. The applied current was 40 mA, and the applied voltage was 45 kV. The X-ray mirror that was used was a graded, flat Bragg−Brentano HD mirror, and the step size that was used for the measurements was 0.0131°. The diffraction patterns were obtained between 5 and 70°. The radiation source used was Cu $K\alpha 1,2$, with Cu $K\alpha 1$ wavelength 1.541 Å and Cu $K\alpha 2$ wavelength 1.544 Å. The ratio of $K\alpha 1/K\alpha 2$ was 0.5. Analysis was performed with a 4 mm mask, 1/8″ incident beam divergence slit, 1/2″ incident beam anti-scatter slit, 7.5 mm diffracted beam anti-scatter slit, and a 0.04 mm Soller slit. The powder was placed on a glass slide and pressed into a 1 cm × 1 cm sized smooth powder film.

Raman Spectroscopy. Raman spectra were acquired using a WITec alpha300R confocal Raman microscope using a 532 nm laser, Zeiss EC Epiplan-Neofluar ×50, G2: 600 g/mm grating, 3 s integration time per point. The spectral range was 100−4000 cm^{-1} with the center at 2000 cm^{-1}, and the spectral resolution was ∼2 cm^{-1}. Before each experiment, the instrument was calibrated using a Si wafer. Laser intensity at the sample was ∼54 mW. Raman mapping of FA-modified HAP was conducted by scanning a grid of 20 × 20 points over a single HAP particle using a 2 s integration time.

Scanning Electron Microscopy. All SEM images were obtained using a Hitachi 4300 SE FE-SEM. A 5.0 kV voltage setting was used with a gun brightness of 1.

X-ray Photoelectron Spectroscopy. The X-ray photoelectron spectroscopy (XPS) spectra were collected using an ex-situ mode in a SPECS near atmospheric pressure XPS (NAP−XPS) system. The NAP−XPS system is equipped with an XR 50 MF Al $K\alpha$ X-ray source with a μ-FOCUS 600 X-ray monochromator. The Al $K\alpha$ radiation was used with an X-ray beam energy of 1486.7 eV and a power of 100 W. A PHOIBOS NAP in situ 1D-DLD hemispherical electron energy analyzer (∼0.85 eV energy resolution and 1 mm entrance aperture) collected the spectra. The pressure during the entire NAP−XPS experiment was always kept at $\sim 10^{-8}$ mbar. Pass energy of 20 eV was utilized unless noted otherwise. Spectral data were processed using the CasaXPS software suite.[21]

Dynamic Vapor Sorption Experiments. The DVS intrinsic (surface measurement systems) was used for all DVS experiments. Sample powder (20 mg) was loaded into the sample pan and exposed to dry airflow (medical grade, RH <2%) for 24 h to remove weakly bound water from the surface. After the drying period, the RH was increased from 0 to 95% and then decreased back to 0% in increments of 5%. During each cycle, the adsorbed mass was recorded as a function of time until the mass change rate (dm/dt) was under 0.002 mg/min where equilibrium was assumed. A probe in the sample chamber was used to constantly measure temperature and maintain a constant 25 °C temperature. The SMS DVS Analysis Suite software package was used to perform data analysis functions such as baseline correction, isotherm calculation, and heat of sorption analysis. HPLC grade water (Millipore-Sigma) was used for all DVS experiments.

Ion Chromatography. Phosphate (PO_4^{3-}) and calcium (Ca^{2+}) ion concentrations were measured using The Metrohm Eco 925 IC system (Herisau, Switzerland). Metrosep A supp 5 (4 × 150 mm) and Metrosep C 4 (4 × 150 mm) separation columns were used to perform anion analysis and cation analysis, respectively. A solution of 3.2 mM Na_2CO_3/1.0 mM $NaHCO_3$ was used as the eluent for PO_4^{3-} ion analysis, whereas a solution of nitric and dipicolinic acid (1.75 nM HNO_3/0.7 mM dipicolinic acid) was the eluent for Ca^{2+} ion analysis. Measurements of all samples were conducted at room temperature and controlled using MagIC Net 3.2 software.

HAP Dissolution Experiments. PO_4^{3-} ion dissolution from HAP was investigated by separately dissolving HAP and FA-modified HAP for 24 and 48 h in citric acid buffer solution with the initial pH values of 5, 6, and 7. 0.15 g of the sample was dissolved in 50 mL of the buffer solution, sealed in a glass chamber, stirred at 250 rpm for 24 h, and the resulting dissolved PO_4^{3-} concentration was measured. Ca^{2+} ion concentrations were also investigated in the same procedures as phosphate except that each sample was dissolved in pH 5 citric acid buffer, and concentrations were measured every 2 h until reaching equilibrium. All sample measurements were conducted at room temperature.

■ RESULTS AND DISCUSSION

Physicochemical Characterization of HAP and FA-Modified HAP. The crystal structures of HAP and the HAP modified using FA for 24 and 48 h were studied using XRD (Figure 1a). The XRD patterns for HAP modified with FA did not exhibit new peaks due to the crystalline modification, indicating that the bulk structure of HAP was not significantly transformed due to FA exposure. In all cases, the HAP crystal structure agreed with previously reported XRD patterns.[22] Since XRD is not able to discriminate between the surface and bulk structure of a material, any surface changes that would occur as a result of FA exposure would not likely be detected via XRD. Therefore, Raman spectroscopy was used as a method of understanding whether the surface of HAP was altered due to FA exposure since a surface overlayer can be detected using this technique.[23] Raman spectroscopy allows for the spatially resolved analysis of the crystals or for the mapping of a select region on a crystal to understand whether FA has modified the HAP crystal. Figure 1b shows the Raman spectra for select spots on the HAP and FA-modified HAP crystals. All samples exhibit a symmetric ν_1 phosphate stretch located at 960 cm^{-1}, as well as the asymmetric ν_3 phosphate stretch located at 1050 cm^{-1}.[24] The ν_2 O−P−O bending mode is located at 428 cm^{-1} and the ν_4 mode at 585 cm^{-1}.[24] A small sharp peak at 3579 cm^{-1} corresponds to the OH stretching mode.[24] In the case of FA-modified HAP, additional peaks at 1356, 1392, 2880, and 2900 cm^{-1} were observed. These peaks are attributed to the formation of $Ca(HCOO)_2$ as the FA vapor reacts with HAP and exhibits new C−H and C−O stretching modes.[25,26]

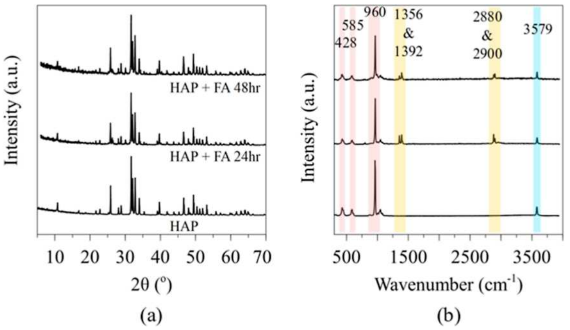

Figure 1. (a)XRD patterns for HAP and FA-modified HAP and (b) Raman spectra for HAP and FA-modified HAP (Raman spectra correspond to single-spot acquisitions).

While Raman spectra acquired at select spots for the FA-modified HAP suggested the formation of $Ca(HCOO)_2$, to investigate the spatial distribution of new Raman signals over the particles, Raman mapping was used. Figure 2a,b shows the optical confocal images of HAP particles exposed to FA for 24 and 48 h, respectively. Figure 2c,d shows the spatial distribution of the 960, 1356, 1392, 2800, 2900, and 3541 cm^{-1} peaks across the highlighted area on the particle (as shown by the red rectangle in Figure 2a,b). Importantly, the 1356 and 1392 peaks, as well as the 2800 and 2900 peaks, are all co-localized over the same area on the map. This suggests that this area corresponds to $Ca(HCOO)_2$ formation as previous studies have shown that FA adsorption on HAP (010) occurs through the transfer of the acidic proton on FA to the surface and HCO^- bonding to the surface Ca site.[19,25,26] Since the confocal Raman analysis depth is several hundred nanometers into the crystal, HAP parent structure peaks were detected in the areas where $Ca(HCOO)_2$ was detected, as shown in the combined images. Raman mapping indicates the formation of $Ca(HCOO)_2$ on the HAP particles but localized to distinct parts of the HAP particles.

Figure 3 shows the SEM images for HAP and FA-modified HAP. HAP particles exhibit a wide size range and do not have a well-defined shape. The FA exposure did not lead to significant morphological changes in the HAP particles.

XPS Analysis of HAP and FA-Modified HAP. The surface region properties within the elastically scattered photoelectron escape depth of a few nanometers of HAP and FA-modified HAP were studied using XPS. Figure 4 shows the XPS spectra for O 1s, Ca 2p, C 1s, and P 2p regions for HAP and the FA-modified HAP. The O 1s peak is centered around 530.8 eV and shifts to 531.5 eV with exposure to FA for 48 h. The Ca 2p regions are shown with the Ca $2p_{3/2}$ peak centered at 347.0 eV for untreated HAP but shifts to higher binding energy with FA exposure. The P 2p peak for HAP is centered around 132.9 eV, consistent with previous reports.[27,28] For FA-exposed HAP samples, the 48 h exposed sample also exhibited a peak shift to a higher binding energy side. For untreated HAP, the C−C peak is centered around 285.0 eV (also used for charge calibration of the XPS data), while the O═C−O is centered around 288.8 eV, agreeing with previous studies.[28] The intensity of the O═C−O peak with respect to the C−C peak at 285.0 eV increases with longer exposure times to FA. The major $Ca(HCOO)_2$ peak is centered around 288.8 eV.[29] As the HAP is exposed to FA vapor, the formation of $Ca(HCOO)_2$ leads to the O═C−O region growing, which is similar to observations seen on $CaCO_3$ surfaces exposed to FA vapor.[29] XPS data suggest the growth of an organic Ca-salt overlayer, as observed in this study, and are consistent with observations reported on $CaCO_3$ with FA as well as other studies on acetic acid adsorption on MgO.[29,30]

Water Sorption on HAP and FA-Modified HAP as a Function of Relative Humidity. The water sorption properties of HAP and FA-modified HAP were studied using DVS. Before water vapor sorption, HAP samples were pretreated by flowing dry air for 24 h to remove weakly physisorbed water molecules from the surface according to similar procedures for non-hygroscopic materials, including HAP.[20,31,32] To preserve the native surface of HAP (and FA-modified HAP) that would be observed under environmentally relevant conditions, the 24 h drying pretreatment is used instead of high-temperature or vacuum treatments that would alter the surface properties that would be observed in the natural state of HAP. HAP demonstrated a type II isotherm for

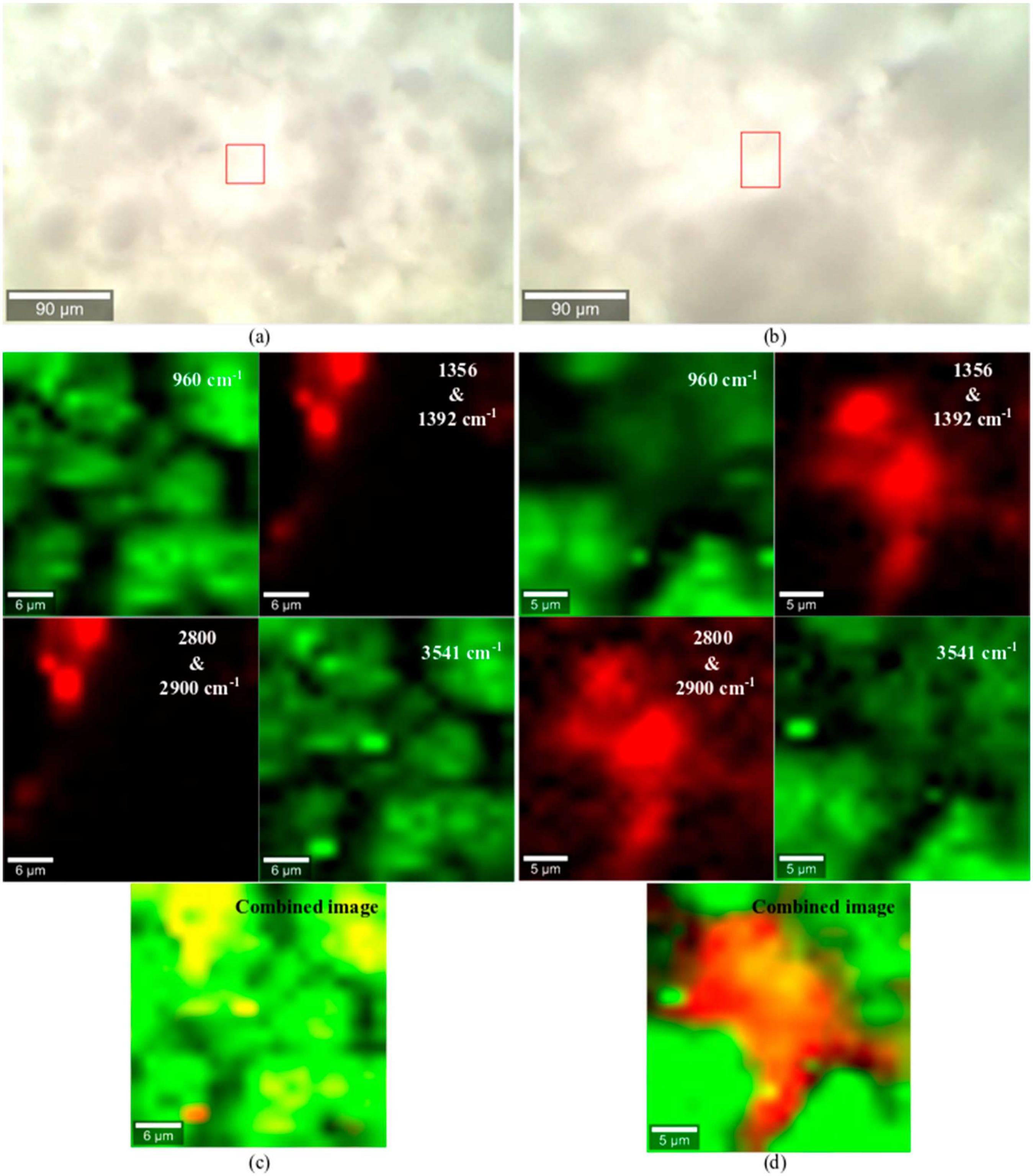

Figure 2. Optical images for (a) HAP + FA 24 h and (b) HAP + FA 48 h (the red square denotes the area over which the mapping was performed). Raman maps for (c) HAP + FA 24 h and (d) HAP + FA 48 h show select peaks and their spatial distribution over the particle in the mapped area and the combined images.

the adsorption branch (Figure 5a), in agreement with the literature.[17]

Type II behavior arises from unrestricted monolayer–multilayer adsorption.[33] Both HAP and FA-modified HAP do not display a clear transition point where the monolayer transitions into a multilayer. An H3 type hysteresis loop was observed both in HAP, as well as FA-modified HAP (both 24 and 48 h exposures), which indicates a deviation from true type II behavior in the desorption branch. This is reported to be caused by the metastability of the adsorbed multilayer.[34] All three cycles of adsorption/desorption on untreated HAP show consistent behavior with no change in the adsorbed water

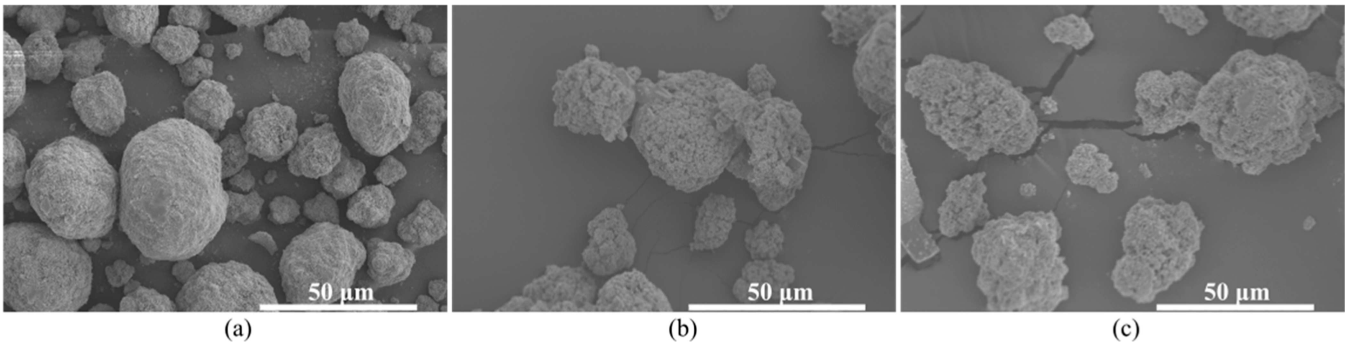

Figure 3. SEM images of (a) HAP, (b) HAP + FA 24 h, and (c) HAP + FA 48 h.

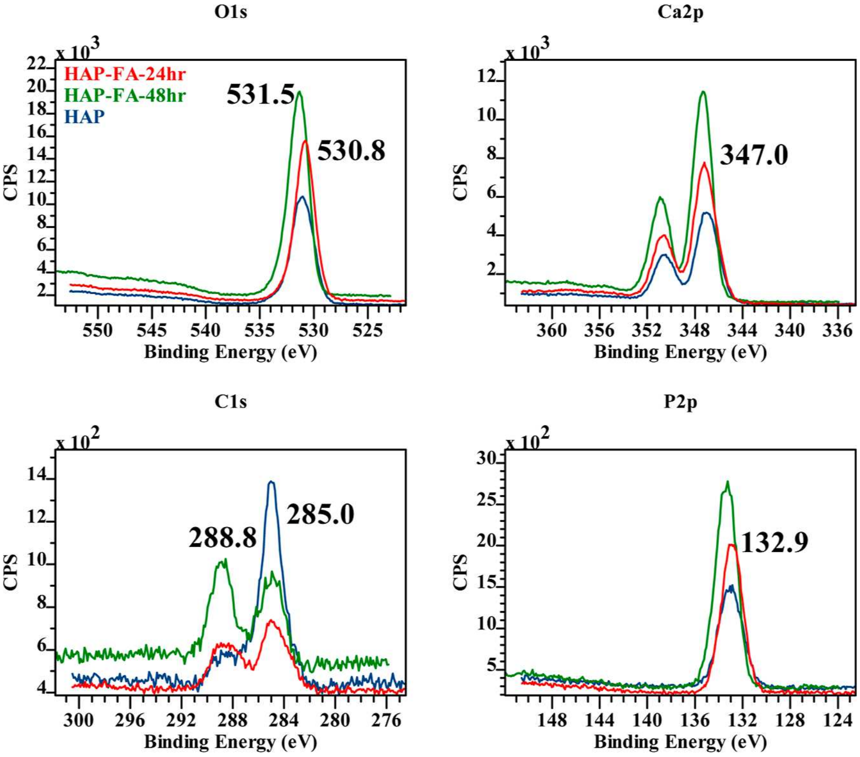

Figure 4. XPS spectra for (a) O 1s, (b) Ca 2p, (c) C 1s , and (d) P 2p regions.

amount. FA-modified HAP exhibits a hysteresis loop that becomes wider with longer FA exposure. Permanent hysteresis is in general attributed to adsorption layer metastability and/or pore network effects such as capillary condensation.[33] However, since the porosity in HAP is attributed to the presence of macropores, the hysteresis may be caused by the pore condensate not filling the macropores.[33,35,36] Compared to the HAP isotherms, the hysteresis loop widens in the case of HAP exposed to FA for 24 h (Figure 5b), with the 48 h exposed HAP showing the widest hysteresis loop and a higher water uptake at 95% RH. Untreated HAP exhibits a maximum relative mass change of 0.4% at 95% RH exposure in cycle 1, while the HAP samples exposed to FA for 24 and 48 h exhibit maximum uptakes of 0.82 and 3.26%, respectively, in cycle 1. The increase in the water uptake as a function of exposure time to FA indicates the formation of $Ca(HCOO)_2$ on HAP particles, which are significantly more soluble compared to HAP.[37] As shown in Figure 5d, $Ca(HCOO)_2$ leads to 0.73% maximum water uptake at 95%, compared to the 0.4% of HAP, indicating that $Ca(HCOO)_2$ is more hygroscopic. As the more soluble component $Ca(HCOO)_2$ adsorbs more moisture content during the higher RH levels (≥80%) a higher overall water uptake of the composite particle is expected. As the HAP is exposed to FA for longer periods, a larger fraction of its surface is expected to be converted to $Ca(HCOO)_2$. This is also possibly a contributing factor to the growing hysteresis as the dissolution of these $Ca(HCOO)_2$ regions would contribute to the widening hysteresis loop observed in both FA-treated HAP samples compared to untreated HAP. These findings are consistent with previous reports demonstrating that hydrated formates of Ca and Mg can exhibit highly hygroscopic behavior at high RH due to the amorphous nature of the formate phase.[38] If such amorphous formate domains are being formed on the HAP surface in this work, the increased uptake of water at RH greater than 90% can be attributed to these surface domains. These observations indicate that longer FA processing times of mineral dust can potentially increase their hygroscopicity, which may have important implications for their nutrient release into the environment. This effect of altered hygroscopicity in composite materials has been

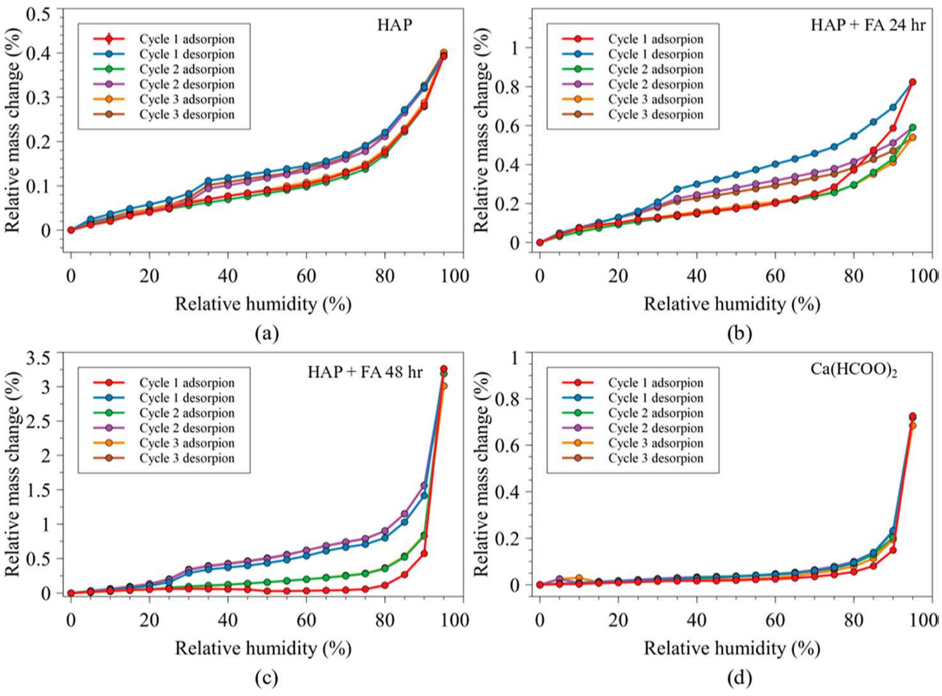

Figure 5. Water adsorption isotherms on (a) HAP, (b) HAP exposed to a 20% FA aqueous solution saturated vapor for 24 h, (c) HAP exposed to a 20% FA solution saturated vapor for 48 h, and (d) commercial $Ca(HCOO)_2$ [(a) data taken from the previous study.[20]

reported in ternary and binary co-crystals between highly soluble urea and sparingly soluble materials such as thiourea,[39] salicylic acid,[40] and gypsum,[41] which in turn alter their nutrient release rates.

BET Analysis of Water Sorption on HAP and FA-Modified HAP. The BET model is one of the most widely used equations in the analysis of the surface area, pore texture, and fitting sorption data for a variety of molecules.[33,42] Previous reports on the use of the BET equation have stated that in the case of type II isotherms with a linear region and reasonable ($20 < C < 100$) C values, the BET equation provides accurate data, while for $C < 20$, a clear monolayer/multilayer distinction is difficult.[43] Water sorption on environmentally relevant mineral interfaces such as clays and fly ashes has been analyzed using the BET equation.[31,32,44,45] In this work, the BET equation is used to calculate the monolayer coverage of water and surface area of HAP and FA-modified HAP during the adsorption branch (Figure 6). Equation 1 shows the BET equation used for monolayer coverage calculation.

$$\frac{1}{V_a\left(\frac{P_0}{P}-1\right)} = \frac{C-1}{V_m C}\cdot\frac{P}{P_0} + \frac{1}{V_m C} \tag{1}$$

The P/P_0 variable signifies the relative pressure of the adsorbate molecule of interest, which varied from 0 to 0.95. The range of data between 0.05 and 0.35 was used for fitting the linear BET equation as this region is typically treated at that of monolayer formation.[33] The parameters V_a and V_m denote the volume of adsorbed molecules and the specific monolayer capacity, respectively. The C parameter is a BET sorption constant, which is exponentially related to the monolayer adsorption energy.[33] The BET-specific surface area was calculated using a molecular cross-sectional area of 0.125 nm^2 for a water molecule.[46]

BET fits for untreated HAP across all three cycles resulted in monolayer capacities between 3.0×10^{-5} and 4.3×10^{-5} mol/g, and the BET surface area (S_{BET}) varied between 1.83 and 2.74 m^2/g. The R^2 values for the fits varied between 0.91 and 1.00. HAP exposed to FA for 24 h exhibited monolayer capacities between 3×10^{-5} and 8×10^{-5} mol/g, and the S_{BET} varied between 1.83 and 4.9 m^2/g. The R^2 values for the first ranged between 0.97 and 1.00. Finally, HAP exposed to FA for 48 h showed monolayer capacities between 4.1×10^{-5} and 6.4×10^{-5} mol/g, and the S_{BET} varied between 2.57 and 4.1 m^2/g. The R^2 values for the first ranged between 0.94 and 1.00. In all three cases, the C value was calculated to be greater than unity, which confirms the type II multilayer adsorption behavior of water on HAP and FA-modified HAP.[32] The two HAP samples exposed to FA for 24 and 48 h exhibit increasing monolayer coverage with each subsequent cycle, indicating that the presence of the more soluble $Ca(HCOO)_2$ overlayer is lending to more water sorption, potentially by forming a saturated liquid layer at high RH values, as discussed in previous literature reports.[47] While no bulk particle deliquescence occurs, the surface of the material may undergo slight dissolution to form a liquid overlayer in the multilayer adsorption regime.[47,48] This may lead to the observed increase in monolayer capacity and overestimation of surface area.

Freundlich Analysis of Water Sorption on HAP and FA-Modified HAP. The Freundlich equation has been applied over a wide variety of adsorption reactions, and it is applicable for both solid−liquid and solid−gas interfaces.[32,49−51] This empirical equation is used to model the adsorption of gas molecules on a heterogeneous surface with an exponential energy distribution of adsorption.[52] The Freundlich equation is shown using eq 2.

$$\frac{x}{m} = K_F\left(\frac{P}{P_0}\right)^{1/n} \tag{2}$$

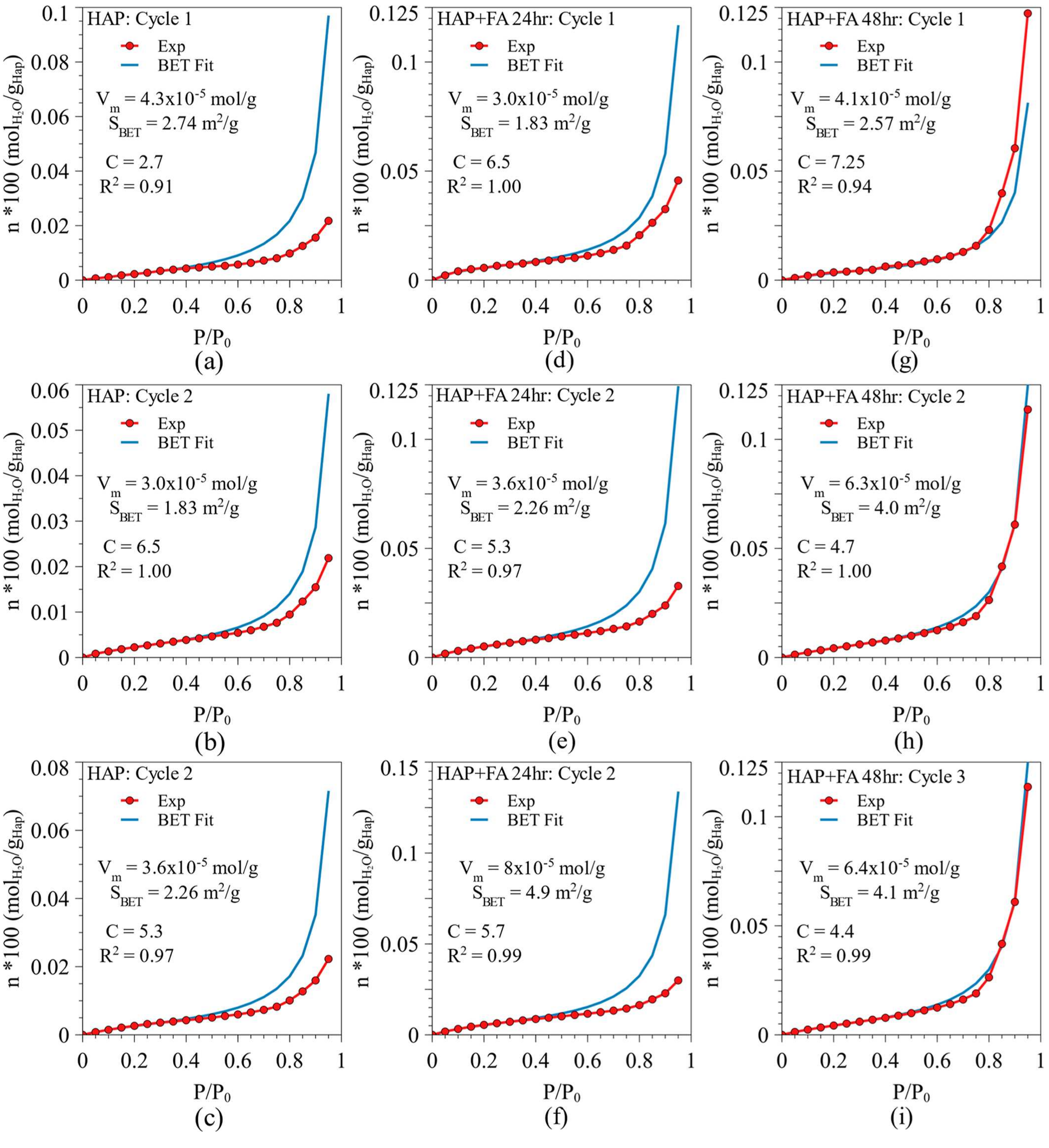

Figure 6. BET fits for (a–c) HAP, (d–f) HAP + FA 24 h, and (g–i) HAP + FA 48 h [(a–c) data taken from the previous study.[20]

The K_F term denotes a Freundlich equilibrium constant, whereas n denotes a fitting coefficient that is indicative of the binding affinity on the adsorbent surface. The K_F term is dependent on temperature. The terms x and m denote the mass change (in mg) and the total dry sample mass (in mg), whereas P/P_0 denotes the relative pressure of the adsorbate gas. The Freundlich equation was applied to the two linear regions in the low RH region (0–25%) and high RH range (25–60%), as shown in Figure 7. Across all three samples, the Freundlich equation fits the adsorption data with high R^2 values ($R^2 > 0.98$), indicating that the Freundlich equation models the adsorption data in both linear ranges well.

As the Freundlich model is based on the assumption that the adsorbent surface interactions with the adsorbate molecules are heterogeneous, the fit is believed to be improved compared to the BET model, which assumes homogeneous behavior. Untreated HAP shows good agreement with the Freundlich model in both linear regions 0–20 and 25–60% with R^2 values equal to or above 0.99. The K_F parameters for HAP in the 0–20% RH region of cycles 1, 2, and 3 were 1.0×10^{-2}, 7.7 ×

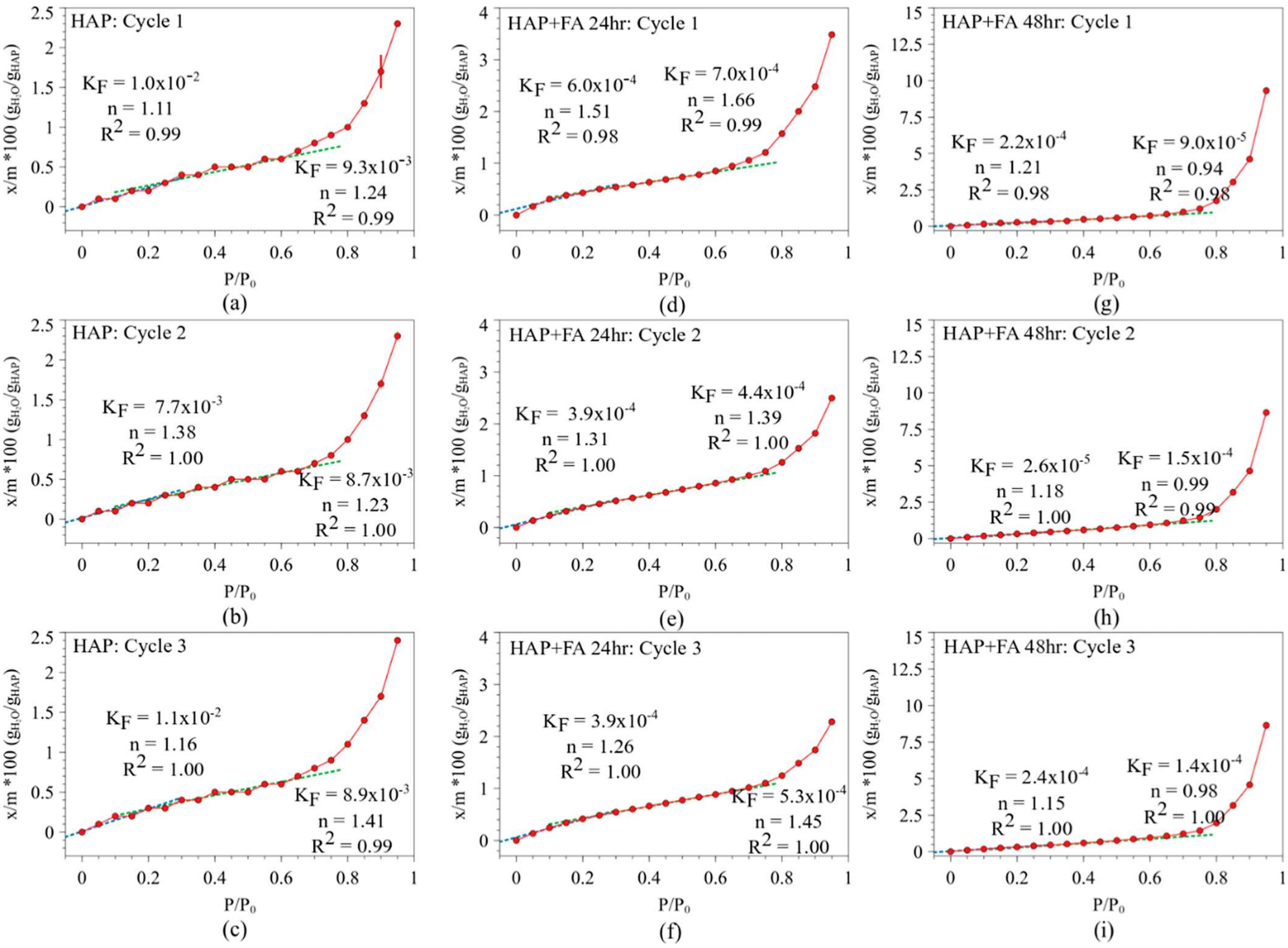

Figure 7. Freundlich fits for (a−c) HAP, (d−f) HAP + FA 24 h, and (g−i) HAP + FA 48 h [(a−c) data taken from the previous study.[20]

Table 1. Tabulated K_F and *n* Values Obtained for the Freundlich Model Fits in Linear Regions of 0−20 and 25−60%

		K_F		N	
	cycle	0−20% RH	25−60%	0−20% RH	25−60%
HAP	1	1.0×10^{-2}	9.3×10^{-3}	1.11	1.24
	2	7.7×10^{-3}	8.7×10^{-3}	1.38	1.23
	3	1.1×10^{-2}	8.9×10^{-3}	1.16	1.41
HAP + FA 24 h	1	6.0×10^{-4}	7.0×10^{-4}	1.51	1.66
	2	3.9×10^{-4}	4.4×10^{-4}	1.31	1.39
	3	3.9×10^{-4}	5.3×10^{-4}	1.26	1.45
HAP + FA 48 h	1	2.2×10^{-4}	9.0×10^{-5}	1.21	0.94
	2	2.6×10^{-5}	1.5×10^{-4}	1.18	0.99
	3	2.4×10^{-4}	1.4×10^{-4}	1.15	0.98

10^{-3}, and 1.1×10^{-2}, respectively. The K_F parameters in the 25−60% RH range for cycles 1, 2, and 3 were 9.3×10^{-3}, 8.7×10^{-3}, and 8.9×10^{-3}, respectively. The *n* parameters for the 0−20% region in HAP in cycles 1, 2, and 3 are 1.11, 1.38, and 1.16, while in the 25−60% region are 1.24, 1.23, and 1.41. For HAP exposed to FA for 24 h, the K_F parameters in the 0−20% RH region of cycles 1, 2, and 3 were 6.0×10^{-4}, 3.9×10^{-4}, and 3.9×10^{-4}, respectively. The K_F parameters in the 25−60% RH range for cycles 1, 2, and 3 were 7.0×10^{-4}, 4.4×10^{-4}, and 5.3×10^{-4}, respectively. The *n* parameters for the 0−20% region in cycles 1, 2, and 3 are 1.51, 1.31, and 1.26, while in the 25−60% region are 1.66, 1.39, and 1.45. Finally, for HAP exposed to FA for 48 h, the K_F parameters in the 0−20% RH region of cycles 1, 2, and 3 were 2.2×10^{-4}, 2.6×10^{-5}, and 2.4×10^{-4}, respectively. The K_F parameters in the 25−60% RH range for cycles 1, 2, and 3 were 9.0×10^{-5}, 1.5×10^{-4}, and 1.4×10^{-4}, respectively. The *n* parameters for the 0−20% region in HAP in cycles 1, 2, and 3 are 1.21, 1.18, and 1.15, while in the 25−60% region are 0.94, 0.99, and 0.98. These are summarized in Table 1. Typically, an *n* value greater than 1 describes a strong interaction between the surface and the adsorbate. In contrast to HAP and HAP exposed to FA for 24 h, the HAP exposed to FA for 48 h shows an *n* parameter lower than 1, indicating that in the multilayer regime, water is not tightly bound to the surface. As discussed in the previous section, water forming a saturated solution on the surface of

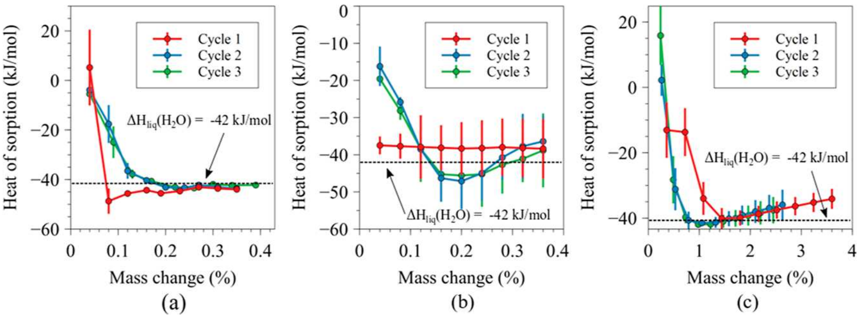

Figure 8. Heat of sorption (kJ/mol) as a function of mass change (%) for (a) HAP, (b) HAP + FA 24 h, and (c) HAP + FA 48 h. (HAP heat of sorption data taken from the previous study[20]). Phosphate (PO_4^{3-}) and calcium (Ca^{2+}) ion dissolution from HAP and FA-modified HAP.

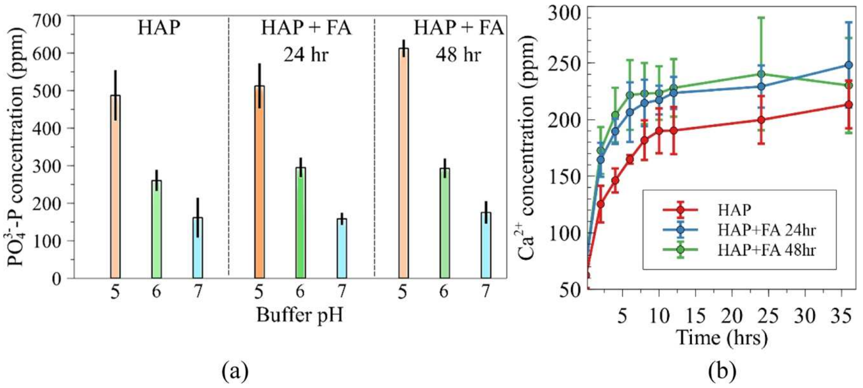

Figure 9. (a) Phosphate (PO_4^{3-}) ion concentrations in solution dissolved from HAP and FA-modified HAP under initial pH values of 5, 6, and 7 in citric acid buffer solutions after 24 h of dissolution. (b) Calcium (Ca^{2+}) ion concentrations in solution dissolved from HAP and FA-modified HAP in pH 5 citric acid buffer.

the particles facilitated by the $Ca(HCOO)_2$ dissolution may lead to this behavior as well as in the decreasing K_F term with increased formic acid exposure.

Heat of Sorption Analysis of Water Sorption on HAP and FA-Modified HAP. The heat of sorption for water adsorption on HAP and FA-modified HAP was calculated using the Clausius−Clapeyron equation, as shown using eq 3.

$$\ln\left(\frac{P_1}{P_2}\right) = \frac{-\Delta H_{ads}}{R}\left(\frac{1}{T_1} - \frac{1}{T_2}\right) \tag{3}$$

The heat of sorption was calculated using the adsorption data for each cycle (Figure 8). The heat of sorption for an adsorption process can be calculated if the two pressure values (P_1 and P_2) are known for two temperature values (T_1 and T_2). R denotes the universal gas constant, and ΔH_{ads} denotes the isosteric heat of sorption. Figure 8a shows the heat of sorption for HAP. The heat of sorption for HAP stays relatively consistent between all three cycles, and as the coverage of water increases, the heat of adsorption approaches the heat of liquefaction of water. As shown by the previous literature, water sorption before the formation of a monolayer shows a trend of the heat of sorption becoming more negative, and as the transformation from monolayer to multilayer occurs, the heat of sorption reaches a plateau. Previous work on HAP and ZnO has shown similar trends.[53,54] The HAP sample exposed to FA for 24 h approaches the heat of liquefaction under 0.4% mass change, similar to HAP, but the 48 h exposed sample approaches this value around 1% mass change and continues a slight upward trend up to 3.6% in the first cycle and then 2.6% in subsequent cycles. Due to the higher water uptake on the HAP exposed to FA for 48 h, the multilayer formation may be occurring later compared to untreated HAP, leading to the heat of sorption converging at higher mass change values.

Dissolution of HAP particles in aqueous solutions of citric acid was carried out to simulate the soil effects on phosphorus availability. Citric acid is exuded by the plant roots and contributes to phosphate availability in the plants.[55,56] In the first step of investigating the simulated atmospheric processing effect with FA on PO_4^{3-} ion release, dissolution experiments were performed at pH of 5, 6, and 7 for 24 h of dissolution. The results are shown in Figure 9a. It can be seen that at lower pH of 5, there is a statistically significant increase in dissolved PO_4^{3-} ion amount from 500 to 600 ppm for HAP modified with FA for 48 h. While the PO_4^{3-} ion dissolution in citric acid-buffered solutions was equilibrium limited and enhanced by the FA processing of HAP, measurement of dissolved Ca^{2+} showed kinetically dependent behavior, as shown in Figure 9b. In particular, there was a statistically significant enhancement in Ca^{2+} ion dissolution in the early stages of the experiment while under equilibrium, dissolved Ca^{2+} ion concentration approached the same 240 ppm. It can be proposed that $Ca(HCOO)_2$ particles, formed on the HAP surface, facilitate Ca^{2+} ion dissolution kinetics in the early stage of the experiment before equilibrium is approached. Collectively, the data shown in Figure 9 suggest the profound effect of the atmospheric processing with FA on the enhanced availability of nutrients, both P and Ca, after HAP deposition in soil.

CONCLUSIONS AND ENVIRONMENTAL IMPLICATIONS

Water sorption properties of mineral dust and other environmentally relevant mineral interfaces provide valuable insights into understanding how critical nutrients can enter the nutrient cycles.[11,14,40] The water sorption properties of HAP were altered by FA vapor exposure as the hygroscopicity of HAP particles increased, with increasing FA exposure time. This was attributed to the formation of distinct $Ca(HCOO)_2$ particles on the surface of HAP particles, leading to the overall hygroscopicity of the composite particle increasing due to the soluble nature of $Ca(HCOO)_2$. The formation of such $Ca(HCOO)_2$ domains was confirmed using spatially resolved Raman mapping and XPS studies. BET model fitting of the water sorption isotherms showed that the water monolayer capacity increased over subsequent adsorption cycles on the FA-exposed HAP, indicating that the dissolution of the soluble $Ca(HCOO)_2$ surface may be contributing to the increased monolayer capacity despite the particles themselves not undergoing bulk deliquescence. The heat of sorption analysis showed that in all three cases, the heat of sorption approached the heat of water liquefaction with increasing water adsorption, but for the HAP exposed to FA for 48 h, the heat of sorption converged at mass change values higher than those of HAP or HAP exposed to FA for 24 h. This study shows that acid processing of apatite minerals has a significant impact on the hygroscopicity and water sorption properties of mineral particles due to the surface modification, indicating that acid processing of mineral apatite dust particles may have significant environmental implications for nutrient cycling, especially the P-cycle.

AUTHOR INFORMATION

Corresponding Author

Jonas Baltrusaitis – *Department of Chemical and Biomolecular Engineering, Lehigh University, Bethlehem, Pennsylvania 18015, United States;* orcid.org/0000-0001-5634-955X; Phone: +1-610-758-6836; Email: job314@lehigh.edu

Authors

Manoj Silva – *Department of Chemical and Biomolecular Engineering, Lehigh University, Bethlehem, Pennsylvania 18015, United States;* orcid.org/0000-0002-5353-006X

Mohamed Eisa – *Department of Chemical and Biomolecular Engineering, Lehigh University, Bethlehem, Pennsylvania 18015, United States;* orcid.org/0000-0001-8821-2005

Dovilė Ragauskaitė – *Department of Chemical and Biomolecular Engineering, Lehigh University, Bethlehem, Pennsylvania 18015, United States;* orcid.org/0000-0002-5353-3391

Complete contact information is available at: https://pubs.acs.org/10.1021/acsearthspacechem.2c00273

Notes

The authors declare no competing financial interest.

ACKNOWLEDGMENTS

This material is based upon work supported by the National Science Foundation under grant no. CHE 1710120.

REFERENCES

(1) Baltrusaitis, J.; Usher, C. R.; Grassian, V. H. Reactions of Sulfur Dioxide on Calcium Carbonate Single Crystal and Particle Surfaces at the Adsorbed Water Carbonate Interface. *Phys. Chem. Chem. Phys.* **2007**, *9*, 3011–3024.

(2) Chen, H.; Navea, J. G.; Young, M. A.; Grassian, V. H. Heterogeneous Photochemistry of Trace Atmospheric Gases with Components of Mineral Dust Aerosol. *J. Phys. Chem. A* **2011**, *115*, 490–499.

(3) Kumar, P.; Nenes, A.; Sokolik, I. N. Importance of Adsorption for CCN Activity and Hygroscopic Properties of Mineral Dust Aerosol. *Geophys. Res. Lett.* **2009**, *36*, L24804.

(4) Kim, D.; Xiao, Y.; Karchere-Sun, R.; Richmond, E.; Ricker, H. M.; Leonardi, A.; Navea, J. G. Atmospheric Processing of Anthropogenic Combustion Particles: Effects of Acid Media and Solar Flux on the Iron Mobility from Fly Ash. *ACS Earth Space Chem.* **2020**, *4*, 750–761.

(5) Molina, M. J.; Molina, L. T.; Kolb, C. E. Gas-Phase and Heterogeneous Chemical Kinetics of the Troposphere and Stratosphere. *Annu. Rev. Phys. Chem.* **1996**, *47*, 327–367.

(6) Paytan, A.; McLaughlin, K. The Oceanic Phosphorus Cycle. *Chem. Rev.* **2007**, *107*, 563–576.

(7) Usher, C. R.; Michel, A. E.; Grassian, V. H. Reactions on Mineral Dust. *Chem. Rev.* **2003**, *103*, 4883–4940.

(8) Romanías, M. N.; Ourrad, H.; Thévenet, F.; Riffault, V. Investigating the Heterogeneous Interaction of VOCs with Natural Atmospheric Particles: Adsorption of Limonene and Toluene on Saharan Mineral Dusts. *J. Phys. Chem. A* **2016**, *120*, 1197–1212.

(9) Atkinson, R.; Arey, J. Atmospheric Degradation of Volatile Organic Compounds. *Chem. Rev.* **2003**, *103*, 4605–4638.

(10) Xue, Y.; Huang, Y.; Ho, S.; Chen, L.; Wang, L.; Lee, S.; Cao, J. Origin and Transformation of Ambient Volatile Organic Compounds during a Dust-to-Haze Episode in Northwest China. *Atmos. Chem. Phys.* **2020**, *20*, 5425–5436.

(11) Stockdale, A.; Krom, M. D.; Mortimer, R. J. G.; Benning, L. G.; Carslaw, K. S.; Herbert, R. J.; Shi, Z.; Myriokefalitakis, S.; Kanakidou, M.; Nenes, A. Understanding the Nature of Atmospheric Acid Processing of Mineral Dusts in Supplying Bioavailable Phosphorus to the Oceans. *Proc. Natl. Acad. Sci. U.S.A.* **2016**, *113*, 14639–14644.

(12) Dam, T. T. N.; Angert, A.; Krom, M. D.; Bigio, L.; Hu, Y.; Beyer, K. A.; Mayol-Bracero, O. L.; Santos-Figueroa, G.; Pio, C.; Zhu, M. X-Ray Spectroscopic Quantification of Phosphorus Transformation in Saharan Dust during Trans-Atlantic Dust Transport. *Environ. Sci. Technol.* **2021**, *55*, 12694–12703.

(13) Spokes, L. J.; Jickells, T. D.; Lim, B. Solubilisation of Aerosol Trace Metals by Cloud Processing: A Laboratory Study. *Geochim. Cosmochim. Acta* **1994**, *58*, 3281–3287.

(14) Nenes, A.; Krom, M. D.; Mihalopoulos, N.; Van Cappellen, P.; Shi, Z.; Bougiatioti, A.; Zarmpas, P.; Herut, B. Atmospheric Acidification of Mineral Aerosols: A Source of Bioavailable Phosphorus for the Oceans. *Atmos. Chem. Phys.* **2011**, *11*, 6265–6272.

(15) Abeywardana, L.; de Silva, M.; Sandaruwan, C.; Dahanayake, D.; Priyadarshana, G.; Chathurika, J. A .; Karunaratne, N.; Kottegoda, N. Zinc-Doped Hydroxyapatite–Urea Nanoseed Coating as an Efficient Macro–Micro Plant Nutrient Delivery Agent. *ACS Agric. Sci. Technol.* **2021**, *1*, 230–239.

(16) Bell, L. C.; Mika, H.; Kruger, B. J. Synthetic Hydroxyapatite-Solubility Product and Stoichiometry of Dissolution. *Arch. Oral Biol.* **1978**, *23*, 329–336.

(17) Miyauchi, M.; Watanabe, T.; Hoshi, D.; Ohba, T. Irreversible Adsorption of Acidic, Basic, and Water Gas Molecules on Calcium-Deficient Hydroxyapatite. *Dalton Trans.* **2019**, *48*, 17507–17515.

(18) Szałaj, U.; Świderska-Środa, A.; Chodara, A.; Gierlotka, S.; Łojkowski, W. Nanoparticle Size Effect on Water Vapour Adsorption by Hydroxyapatite. *Nanomater* **2019**, *9*, 1005.

(19) Canepa, P.; Chiatti, F.; Corno, M.; Sakhno, Y.; Martra, G.; Ugliengo, P. Affinity of Hydroxyapatite (001) and (010) Surfaces to Formic and Alendronic Acids: A Quantum-Mechanical and Infrared Study. *Phys. Chem. Chem. Phys.* **2011**, *13*, 1099–1111.

(20) Silva, M.; Baltrus, J. P.; Burnett, D. J.; Baltrusaitis, J. Water Adsorption on Hydroxyapatite and Struvite as a Function of Relative Humidity: Application of BET and Freundlich Adsorption Models. *ACS Earth Space Chem.* **2022**, *6*, 431−443.

(21) Fairley, N.; Fernandez, V.; Richard-Plouet, M.; Guillot-Deudon, C.; Walton, J.; Smith, E.; Flahaut, D.; Greiner, M.; Biesinger, M.; Tougaard, S.; Morgan, D.; Baltrusaitis, J. Systematic and Collaborative Approach to Problem Solving Using X-Ray Photoelectron Spectroscopy. *Appl. Surf. Sci. Adv.* **2021**, *5*, 100112.

(22) Chen, K.-Y.; Arai, Y. X-Ray Diffraction and X-Ray Absorption Near-Edge Structure Spectroscopic Investigation of Hydroxyapatite Formation under Slightly Acidic and Neutral PH Conditions. *ACS Earth Space Chem.* **2019**, *3*, 2266−2275.

(23) Kiani, D.; Silva, M.; Sheng, Y.; Baltrusaitis, J. Experimental Insights into the Genesis and Growth of Struvite Particles on Low-Solubility Dolomite Mineral Surfaces. *J. Phys. Chem. C* **2019**, *123*, 25135−25145.

(24) Markovic, M.; Fowler, B. O.; Tung, M. S. Preparation and Comprehensive Characterization of a Calcium Hydroxyapatite Reference Material. *J. Res. Natl. Inst. Stand. Technol.* **2004**, *109*, 553.

(25) Chukanov, N. V.; Menor-Salvan, C.; Gurzhiy, V. V.; Izatulina, A. R.; Pekov, I. V.; Vigasina, M. F.; Ksenofontov, D. A.; Britvin, S. N. Biogenic Orthorhombic α-Calcium Formate from Sediments of Alkali Lake, Oregon, USA. *Minerals* **2021**, *11*, 448.

(26) Eggert, G.; Fischer, A. The Formation of Formates: A Review of Metal Formates on Heritage Objects. *Heritage Sci.* **2021**, *9*, 1−13.

(27) Raikar, G. N.; Ong, J. L.; Lucas, L. C. Hydroxyapatite Characterized by XPS. *Surf. Sci. Spectra* **1996**, *4*, 9.

(28) Uskoković, V. X-Ray Photoelectron and Ion Scattering Spectroscopic Surface Analyses of Amorphous and Crystalline Calcium Phosphate Nanoparticles with Different Chemical Histories. *Phys. Chem. Chem. Phys.* **2020**, *22*, 5531−5547.

(29) Usher, C. R.; Baltrusaitis, J.; Grassian, V. H. Spatially Resolved Product Formation in the Reaction of Formic Acid with Calcium Carbonate (1014): The Role of Step Density and Adsorbed Water-Assisted Ion Mobility. *Langmuir* **2007**, *23*, 7039.

(30) Foster, M.; Passno, D.; Rudberg, J. Fourier Transform Infrared Study of Methanol, Water, and Acetic Acid on MgO(100). *J. Vac. Sci. Technol., A* **2004**, *22*, 1640.

(31) Navea, J. G.; Richmond, E.; Stortini, T.; Greenspan, J. Water Adsorption Isotherms on Fly Ash from Several Sources. *Langmuir* **2017**, *33*, 10161−10171.

(32) Hatch, C. D.; Wiese, J. S.; Crane, C. C.; Harris, K. J.; Kloss, H. G.; Baltrusaitis, J. Water Adsorption on Clay Minerals as a Function of Relative Humidity: Application of BET and Freundlich Adsorption Models. *Langmuir* **2012**, *28*, 1790−1803.

(33) Thommes, M.; Kaneko, K.; Neimark, A. V.; Olivier, J. P.; Rodriguez-Reinoso, F.; Rouquerol, J.; Sing, K. S. W. Physisorption of Gases, with Special Reference to the Evaluation of Surface Area and Pore Size Distribution (IUPAC Technical Report). *Pure Appl. Chem.* **2015**, *87*, 1051−1069.

(34) Sing, K. S. W.; Williams, R. T. Physisorption Hysteresis Loops and the Characterization of Nanoporous Materials. *Adsorpt. Sci. Technol.* **2016**, *22*, 773−782.

(35) Landers, J.; Gor, G. Y.; Neimark, A. V. Density Functional Theory Methods for Characterization of Porous Materials. *Colloids Surf., A* **2013**, *437*, 3−32.

(36) Thommes, M.; Cychosz, K. A. Physical Adsorption Characterization of Nanoporous Materials: Progress and Challenges. *Adsorption* **2014**, *20*, 233−250.

(37) Zhang, Z.; Wang, X.; Ma, J.; Bian, R.; Sui, H.; He, L.; Li, X. Measurement and Correlation of Solubility of Calcium Formate (Form α) in Different Binary Solvent Mixtures at Temperatures from 283.15 to 323.15 K. *J. Chem. Eng. Data* **2019**, *64*, 2475−2483.

(38) Guo, L.; Gu, W.; Peng, C.; Wang, W.; Li, Y.; Zong, T.; Tang, Y.; Wu, Z.; Lin, Q.; Ge, M.; Zhang, G.; Hu, M.; Bi, X.; Wang, X.; Tang, M. A Comprehensive Study of Hygroscopic Properties of Calcium-and Magnesium-Containing Salts: Implication for Hygroscopicity of Mineral Dust and Sea Salt Aerosols. *Atmos. Chem. Phys.* **2019**, *19*, 2115−2133.

(39) Mazzei, L.; Broll, V.; Casali, L.; Silva, M.; Braga, D.; Grepioni, F.; Baltrusaitis, J.; Ciurli, S. Multifunctional Urea Cocrystal with Combined Ureolysis and Nitrification Inhibiting Capabilities for Enhanced Nitrogen Management. *ACS Sustainable Chem. Eng.* **2019**, *7*, 13369−13378.

(40) Silva, M.; Barcauskaite, K.; Drapanauskaite, D.; Tian, H.; Bučko, T.; Baltrusaitis, J. Relative Humidity Facilitated Urea Particle Reaction with Salicylic Acid: A Combined In Situ Spectroscopy and DFT Study. *ACS Earth Space Chem.* **2020**, *4*, 1018−1028.

(41) Barčauskaitė, K.; Brazienė, Z.; Avižienytė, D.; Silva, M.; Drapanauskaite, D.; Honer, K.; Gvildienė, K.; Slinksiene, R.; Jancaitiene, K.; Mazeika, R.; Staugaitis, G.; Dambrauskas, T.; Baltakys, K.; Baltrusaitis, J. Mechanochemically Synthesized Gypsum and Gypsum Drywall Waste Cocrystals with Urea for Enhanced Environmental Sustainability Fertilizers. *J. Environ. Chem. Eng.* **2020**, *8*, 103965.

(42) Brunauer, S.; Emmett, P. H.; Teller, E. Adsorption of Gases in Multimolecular Layers. *J. Am. Chem. Soc.* **1938**, *60*, 309−319.

(43) Sing, K. S. W.; Everett, D. H.; Haul, R. A. W.; Moscou, L.; Pierotti, R. A.; Rouquerol, J.; Siemieniewska, T. Reporting Physisorption Data for Gas/Solid Systems with Special Reference to the Determination of Surface Area and Porosity (Recommendations 1984). *Pure Appl. Chem.* **1985**, *57*, 603−619.

(44) Song, X.; Boily, J.-F. Water Vapor Adsorption on Goethite. *Environ. Sci. Technol.* **2013**, *47*, 7171−7177.

(45) Yeşilbaş, M.; Boily, J. F. Particle Size Controls on Water Adsorption and Condensation Regimes at Mineral Surfaces. *Sci. Rep.* **2016**, *6*, 1−10.

(46) McClellan, A. L.; Harnsberger, H. F. Cross-Sectional Areas of Molecules Adsorbed on Solid Surfaces. *J. Colloid Interface Sci.* **1967**, *23*, 577−599.

(47) Mauer, L. J.; Taylor, L. S. Water-Solids Interactions: Deliquescence. *Annu. Rev. Food Sci. Technol.* **2010**, *1*, 41−63.

(48) Zografi, G. States of Water Associated with Solids. *Drug Dev. Ind. Pharm.* **2008**, *14*, 1905−1926.

(49) Peng, C.; Gu, W.; Li, R.; Lin, Q.; Ma, Q.; Jia, S.; Krishnan, P.; Wang, X.; Tang, M. Large Variations in Hygroscopic Properties of Unconventional Mineral Dust. *ACS Earth Space Chem.* **2020**, *4*, 1823−1830.

(50) Ahmed, S.; Guo, Y.; Huang, R.; Li, D.; Tang, P.; Feng, Y. Hexamethylene Tetramine-Assisted Hydrothermal Synthesis of Porous Magnesium Oxide for High-Efficiency Removal of Phosphate in Aqueous Solution. *J. Environ. Chem. Eng.* **2017**, *5*, 4649−4655.

(51) Freundlich, H.; Heller, W. The Adsorption of Cis- and Trans-Azobenzene. *J. Am. Chem. Soc.* **1939**, *61*, 2228−2230.

(52) Freundlich, H. Of the Adsorption of Gases. Section II. Kinetics and Energetics of Gas Adsorption. Introductory Paper to Section II. *Trans. Faraday Soc.* **1932**, *28*, 195−201.

(53) Nagao, M. Physisorption of water on zinc oxide surface. *J. Phys. Chem.* **1971**, *75*, 3822−3828.

(54) Rootare, H. M.; Craig, R. G. Vapor Phase Adsorption of Water on Hydroxyapatite. *J. Dent. Res.* **1977**, *56*, 1437−1448.

(55) Barrow, N. J.; Debnath, A.; Sen, A. Mechanisms by Which Citric Acid Increases Phosphate Availability. *Plant Soil* **2018**, *423*, 193−204.

(56) Gerke, J. The Acquisition of Phosphate by Higher Plants: Effect of Carboxylate Release by the Roots. A Critical Review. *J. Plant Nutr. Soil Sci.* **2015**, *178*, 351−364.